Graphical Abstract

Optimisation of a Forced Multi-Beam Piezoelectric Energy Harvester

Lucas Q. Machado, Panagiotis Alevras, Dmitri Tcherniak, Junlei Wang, Shengxi Zhou, Daniil Yurchenko

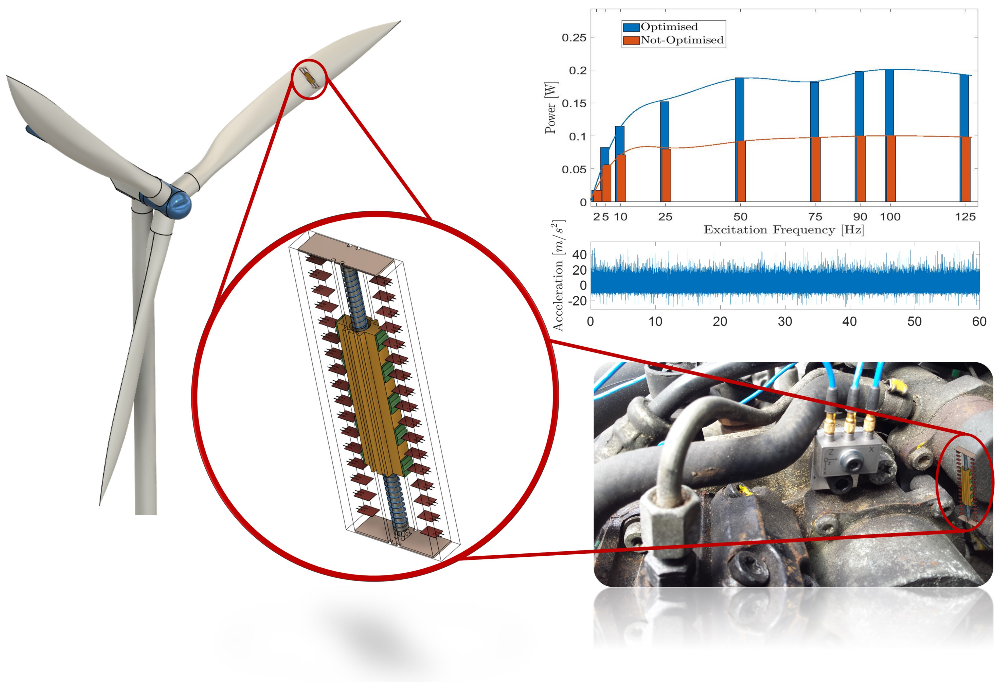

Highlights

Optimisation of a Forced Multi-Beam Piezoelectric Energy Harvester

Lucas Q. Machado, Panagiotis Alevras, Dmitri Tcherniak, Junlei Wang, Shengxi Zhou, Daniil Yurchenko

- Improved design techniques for a device based on arrays of beams.
- Optimised solutions to enable autonomous sensing for two practical case studies.
- Performance analysis and optimisation under a deterministic excitation, a harmonic excitation with random phase modulations and experimental data from practical applications.

Optimisation of a Forced Multi-Beam Piezoelectric Energy Harvester

Lucas Q. Machado[1], Panagiotis Alevras[b], Dmitri Tcherniak[c], Junlei Wang[d], Shengxi Zhou[e], Daniil Yurchenko[f]

[a] *IMPEE, Heriot-Watt University, Edinburgh, UK*
[b] *Department Of Mechanical Engineering, University of Birmingham, Birmingham, UK*
[c] *Hottinger Brüel & Kjær A/S, Virum, Denmark*
[d] *School of Mechanical and Power Engineering, Zhengzhou University, Zhengzhou, China*
[e] *School of Aeronautics, Northwestern Polytechnical University, Xi'an, China*
[f] *IMPEE, ISVR, University of Southampton, Southampton, UK*

Abstract

A high-power multi-beam piezoelectric energy harvesting device is designed to meet the demands of the emerging technologies in Body Sensors Networks (BSNs), Wireless Sensors Networks (WSNs), the Internet of Things (IoT) and the Industrial Internet of Things (IIoTs). The proposed device utilises a plucking mechanism to excite the beams, organised in a comb-like structure. The harvester is presented in different length configurations and its performance is optimised to deliver the highest power under a given set of parameter values, constraints and excitation characteristics. The unique feature of the device is that it can be tuned to any given frequency, although it demonstrates its superior performance in the frequency range of 2-50 Hz, delivering hundreds of mW. The device optimisation is conducted using a harmonic excitation, a harmonic excitation with random phase modulations, experimental data collected from an internal combustion engine, and numerical data from simulation of out-of-plane oscillations of wind turbine blades. The paper proposes solutions to a number of challenges specific for multi-beam structures that have not been addressed before. It is demonstrated for the first time that the proposed harvester is able to meet the demands of relevant sensing applications.

Keywords: Energy Harvesting, Piezoelectricity, Optimisation, Narrow-Band Excitation.

1. Introduction

Energy harvesting (EH) offers versatile and convenient conversion mechanisms when it comes to providing energy to low-power electronics. A device making use of these mechanisms could reduce the dependence of electronics on conventional batteries, extend the batteries' lifespan, and reduce their replacement costs (Machado et al., 2021; Shirvanimoghaddam et al., 2019; Ali et al., 2019; Liu et al., 2018). Thus, the EH technology comes as a response to the demands faced by various industrial sectors. Some potential applications are Body Sensors Network (BSNs), Wireless Sensors Networks (WSNs), the Internet of Things (IoT) and the Industrial Internet of Things (IIoTs) (Sisinni et al., 2018; Gorlatova et al., 2014). Within these applications, potential devices to benefit from energy harvesters are, e.g., pacemakers, hearing aid, GPS receivers, sensors and data transmission nodes. This demand can be successfully met through energy harvesting technology when there is a balance between the harvesting and the required powers. Clearly, different applications have distinct operation routine and require different amount of energy. Thus, understanding the energy profile of an application is the starting point of making a decision if EH is a practical solution and which EH transduction mechanism is more appropriate when considering EH from ambient vibration. A wired strain sensor, for instance, requires 100 μW while a wireless humidity sensor requires 1 mW. However, when the strain sensor operates continuously and the humidity sensor operates with a 10% duty cycle using a ZigBee radio protocol, both of them will have the same energy usage over 24 hours (Sagentia, 2011).

Thus, there is a need for developing harvesters oriented to specific desired solution and efforts have been made towards that. Peigney and Siegert (2013) designed a cantilever piezoelectric energy harvester to operate under bridges' vibrations induced by traffic that was able to deliver a power output of 0.03 mW. They concluded that the harvester could be used to power wireless health monitoring sensor nodes with low duty cycle. Daraji et al. (2021) bonded piezoelectric material to the surface of an aircraft's wing and showed how to optimised its locations for the best power output. It was concluded that this approach would allow powering a device used for signal transmission for environmental monitoring, which requires 22.37 mW. Lee and Choi (2014) proposed an energy harvester to power a wireless sensor required for an intelligent tire system. Their design enabled the device to generate 380 μJ per revolution under 500 kgf load and velocity of 60 km/h.

Usman et al. (2018) proposed a piezoelectric energy harvester excited by the wake galloping phenomena induced by wind. Within energy harvesting from fluid flow, Bao and Wang (2021) proposed a device to harvest the energy from rainfall and were able to charge a 100 μF capacitor within 180 s considering that the rainwater is released from a 24 cm height. No doubt there is a plethora of applications ranging across multiple fields that can benefit from energy harvesting solutions, and are awaiting for the development, practical verification and establishment of this technology into commercialised energy harvester devices.

Some of the main transduction mechanisms used in energy harvesting are piezoelectric, electromagnetic, triboelectric, and electrostatic, which convert mechanical energy into electrical energy via mechanical strain, magnetic induction, frictional contact and electrostatic induction, and varying capacitance, respectively. Among those, the piezoelectric is believed to be the most understood technique, and studies have pointed that it delivers a higher energy density (Pozo et al., 2019; Priya, 2007; Kim et al., 2011; Sezer and Koç, 2021) in the considered specific applications. Piezoelectric technology has matured (Zhou et al., 2020; Alrashdan, 2020), and its versatility allows it to be applied to various industrial sectors. Other attractive advantages are the relatively simple structure of the piezoelectric harvesters (Maghsoudi Nia et al.; Covaci and Gontean, 2020), which facilitates micro- and macro- manufacturing and their integration to micro-electro-mechanical systems (Piliposian et al., 2019; Covaci and Gontean, 2020), they can be embedded into hybrid materials (Maghsoudi Nia et al.) and have adaptable shapes (Cai and Harne, 2019; Peralta et al., 2020; Hashim et al., 2021).

Despite the above mentioned advantages of piezoelectric (PE) energy harvesting, certain factors need to be considered. Firstly, it is unlikely for a single piezoelectric beam device to generate enough energy for existing electronics and sensors, as a limited amount of energy is available in the vast majority of applications and efficiency is low. Moreover, the PE energy harvester performance is highly affected by the excitation frequency. Linear oscillatory systems, such as the piezoelectric generators, are known to yield high energy conversion efficiency only within a narrow band of their resonant frequency. Given the fact that resonance is not always achieved or may not be desired due to high fatigue and potential failure, other techniques have been developed to increase the operating bandwidth of these types of systems by introducing non-linearities (Fu et al. (2021); Fang et al. (2022)), adopting pendulum systems (Izadgoshasb et al., 2019; Ramezanpour et al., 2016), utilising vibroimpact dynamics (Cao et al., 2022; Yurchenko et al., 2017), using the mechanical frequency-up conversion (MFU) (Fu and Yeatman, 2017; Peng et al., 2021; Machado et al., 2021), circuit management (Covaci and Gontean, 2020; Yurchenko et al., 2022), and arrays of beams (Machado et al., 2021; Yurchenko et al., 2022; Lien and Shu, 2013). In recent publication (Machado et al., 2021), a multiple beams harvester was introduced, where the beams were excited by multiple plectra, which can be considered as an improved version of the MFU (Wang et al., 2021; Fu et al., 2021). The multiple plectra design allowed a massive increase in power output, meanwhile significantly complicated the energy harvesting circuit. Piezoelectric harvesters require rectification and output voltage regulation. This becomes a critical factor when dealing with multiple beams, as out-of-phase vibrations lead to charge cancellation. Therefore, an electrical circuit was designed accordingly by Yurchenko et al. (2022), where an energy harvesting circuit solution was able to considerably increase the power output of the system and avoid power cancellation issues in multi-beam harvesters.

Although some efforts towards utilising multi-beam devices has been reported, they have been focused on expanding the bandwidth of EH systems. The device proposed in Machado et al. (2021) was the first device where multiple beams were used for increasing the power density and energy output of the device. The key question addressed in that work was the following: what is the maximum practical amount of power an EH device of a given volume can generate under a specified excitation? To resolve this issue a optimisation approach was proposed and developed in Yurchenko et al. (2022). However, the designed harvester in Machado et al. (2021) was intended for gravity based operation only, where a carriage, sliding on guide rails, plucked beams when the entire device was tilted. Since the distance travelled by the carriage is a design parameter, the device was demonstrating its maximum performance when the half-period of the excitation was equal to the time required for the carriage to cover this distance. Tilting the device with higher frequencies resulted in lower power output since the carriage was not able to engage all the beams. Thus, that device was limited to a relatively low operating frequency range. Obviously, the lower the operating frequency the lower the power output of the device. In this paper, a new design is proposed to enable the device to operate under a forced environment. Here, the host structure of the harvester is connected to a vibration source, thus eliminating the need for tilting or rotating the device. This is achieved by introducing spring-damper elements connecting the carriage to the host structure. The design flexibility allows pre-tuning the device to a wide range of frequencies by adjusting the spring and damping elements, while the carriage mass is selected based on other optimisation criteria.

The paper has the following structure: Section 2 introduces the design of the harvester along with the pertaining technical challenges of the concept adopted. It also discusses an optimisation methodology used to explain the connection between the design parameters and the device's performance. Section 3 presents the response of the harvester given a harmonic excitation input. Three harvester's lengths are analysed under different values of the excitation frequency. Section 4 evaluates the device's performance under a narrow band noise excitation applied to the system. A case study with the harvester operating under real conditions based on the experimental acceleration data collected from an IC engine is presented in Section 5. The second case study, presented in Section 6 demonstrates the harvester performance, inside a wind turbine blade, which provides energy from low frequency out-of-plane oscillations. In Conclusions the outcomes of the conducted analyses are presented.

2. Concept, design challenges and optimisation algorithm

2.1. Concept

The device, designed to operate attached to a vibrating structure, has a length L_d, a width W_d and a thickness t_d as shown in Figure 1. The device's structure transfers mechanical energy into the device's major components: a moving carriage and 2 arrays of identical piezoelectric beams, placed symmetrically at the top and the bottom of the device, as shown in Figure 1a. The carriage comprises a bulk mass, which can move along the device when excited via linear springs, which form the equivalent stiffness of the carriage. Note that there are also damping elements connecting the mass to the host structure, but they are not shown in Figure 1. The carriage has pins/plectra on its both sides, facing the beams. As the carriage oscillates along the guiding rail, pins/plectra pluck the piezoelectric cantilever beams, which are fixed to the host structure, thereby taking advantage of the MFU technique. Note that, in what follows, the discussion is concerned a single array of beams, but it applies to the second array as well.

Within a full cycle, the carriage moves from one side of the host structure to the other one and returns back to its initial position. Figure 1b presents the 3D design of the device where the host structure is shown transparent for

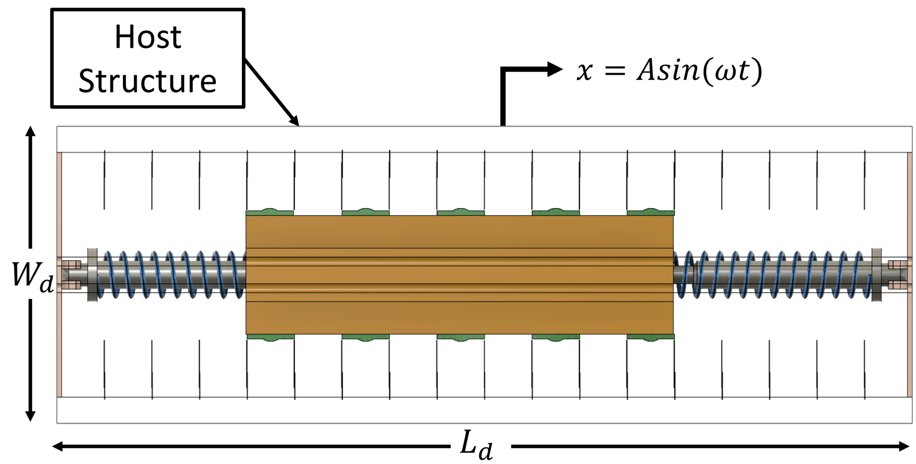

(a)

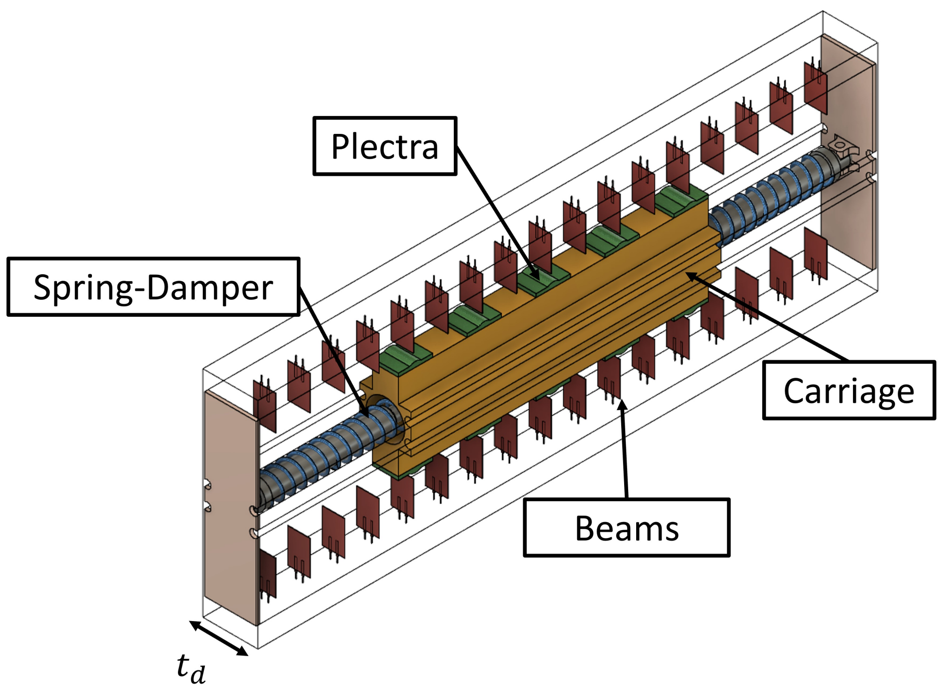

(b)

Figure 1: Device Design: (a) side view presenting the host structure and the excitation direction, and (b) isometric view presenting the main components of the harvester.

the illustration purpose. The proposed design has a number of advantages, as well as some challenges, which are to be discussed in next subsections. The most important advantage of the proposed concept is its ability to be tuned to the excitation frequency, or to a frequency that will lead to the device's best performance. It is well-known that small-sized beams have a relatively high fundamental natural frequency, in a region of several hundreds Hz (the beams used for this study have the fundamental natural frequency over 700Hz), which makes them inappropriate to operate near their resonance since the vast majority of applications have excitation frequencies below 50 Hz.

In view of this challenge, plucking becomes a very useful tool, since the excited beams are vibrating at their fundamental frequency in free vibration, generating a reasonable power output from PE beams. However, their excitation rate depends on the external excitation, which, in the proposed design, comes from the oscillation frequency of the carriage. This frequency can be tuned by adjusting the equivalent stiffness independently, having the carriage's mass been defined from an optimisation procedure earlier in the design process. Moreover, the proposed design assumes that the carriage's displacement covers the entire length on the device. This requirement provides some constrains on the stiffness and damping properties of the mass. Thus, the response amplitude of the carriage becomes an important parameter, which has to be considered by the design. Based on the amplitude-frequency curve, the targeted response amplitude of the carriage can be achieved by two frequency values around the mass's natural frequency. However, to avoid the transition through the resonance, the lower frequency is preferable. Thus, the proposed concept is versatile as its frequency can be independently tuned through the spring's stiffness to a desirable excitation frequency and increased/decreased by adjusting the damping coefficient.

The proposed design process optimises the performance of a given volume device with prescribed layout for a given external excitation, thereby maximising the power of the unit. During this process the power output of the device is determined, which is a function of several interconnected parameters, e.g., the number of piezoelectric beams, the number of plectra, the distance between beams, the number of beams between two plectra, the natural frequency of the beams, the excitation amplitude and frequency of the host structure, natural frequency of the carriage and its damping properties, as well as the overall geometry/space given within the host structure. Some of these parameters are subjected to constrains, which come from physical considerations. For instance, there is a certain number of beams of thickness t_b that can fit inside the device of length L_d. To avoid collision between oscillating adjacent beams, twice the maximum deflection of each beam should be added as the minimal distance between the beams. Thus, the device will have less beams when either their thickness or tip displacement are increased. Thicker beams will generate higher stress and, consequently, higher power output than thinner beams under the same deflection. However, the former require more force to achieve the same deflection, thereby increasing the required carriage mass for a given excitation. An important role in this concept is given to the relationship (A.4) connecting the total number of excitations n_{ex}, the number of beams n_b, the number of plectra n_p and the number of beams between plectra n_{bbp}, established earlier in Machado et al. (2021). This relationship shows a quadratic dependence of the total number of excitation on the number of plectra, which indicates the non-linear increase of excitations with the number of beams and plectra within the device. In addition to that some electrical constraints may be imposed, altogether leading to a multidimensional optimisation problem. To avoid overload and fatigue of the beams, the maximum stress experienced by the PE beams is limited throughout the calculations to $0.75\ \sigma_y$, where σ_y is the yield stress. All the constrains and parameters, as well as the fully coupled electro-mechanical model established and verified experimentally in earlier publications (Machado et al., 2021; Yurchenko et al., 2022) are presented in Appendix A.

2.2. High excitation frequency challenge

One of the critical issues, which may reduce the performance of beams within the device, is the excitation frequency or the ratio between the excitation frequency and the fundamental natural frequency of the piezoelectric beams. Note that the MFU provides more excitations to the beams placed towards the center of the device, i.e., the beams at both ends of the arrays are plucked twice within an excitation period while the beams at the center are plucked $2n_p$. Therefore, the plucking frequency is a leading parameter, as increasing the excitation frequency to a critical level may cause some piezoelectric beams to have a very small or no oscillations between pluckings, practically remaining in a quasi-static equilibrium position generating negligible power.

Figure 2 presents the electro-mechanical response of the device during the carriage's half-period displacement under different excitation frequencies. In

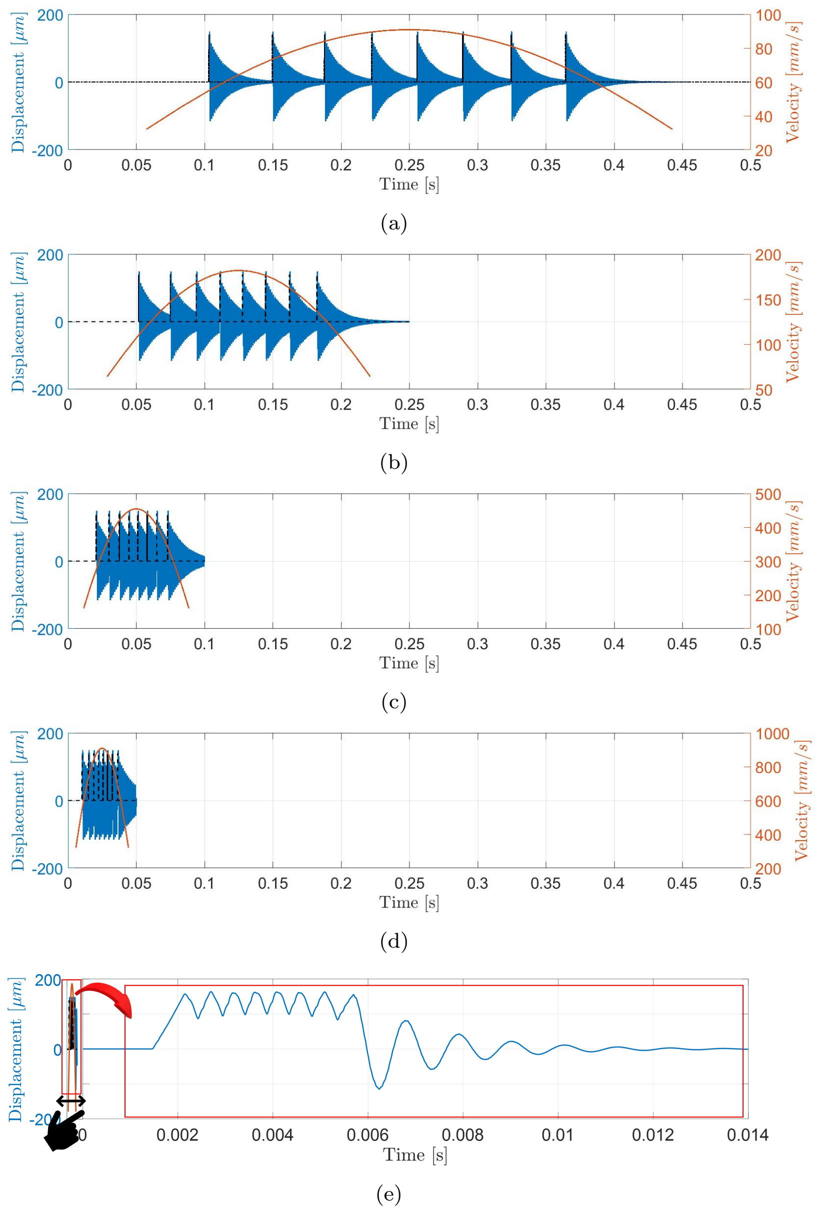

Figure 2: Harvester response to excitation at (a) 1 Hz, (b) 2 Hz, (c) 5 Hz, (d)10 Hz, (e) 70 Hz without constraint applied.

this example there are 46 beams in total, 8 plectra, and 3 beams between each plectrum. The charts present the response of the 23rd beam, placed in the middle of the device and excited most frequently. Note that due to the sinusoidal displacement, the time frame between pluckings is longer at the start and the end of the half-period, while it is shorter in the middle part as a result of the carriage's velocity, indicated by the red curve in all the charts in Figure 2. As it can be seen from Figure 2a and Figure 2b, low excitation frequencies (1 Hz and 2 Hz respectively), allow the beam to oscillate several periods before it is plucked again by another plectrum as the carriage keeps moving on. As the excitation frequency increases, the time between two subsequent pluckings decreases, as shown in Figure 2c and Figure 2d.

A critical scenario is presented in Figure 2e, where the excitation frequency is $f = 70Hz$. A closer look at the carriage's half-period reveals that in this case the beam is being plucked before it can complete its natural half-period. Further increasing the excitation frequency can lead to the limiting case when the carriage's speed is high enough to keep the beam near a quasi-static deflected position, thus generating almost no charge. To avoid this issue a constraint (1) can be imposed:

$$d_{bp} \geq \frac{f_c(L_d - L_M)}{4f_b}, \tag{1}$$

where f_c is the carriage frequency, d_{bp} is the distance between two plectra, f_b is the fundamental natural frequency of the beam, L_M is the carriage length. This constraint increases the number of beams between plectra in a way that the minimum allowed time between pluckings is equal to the beam's half-period. This allows the beams to vibrate longer at the cost of less excitations. Note that the operation frequency of 70 Hz is critical for the example presented here. The phenomena discussed in this scenario may occur at lower or higher frequencies depending on the characteristics and parameters of the device. All analyses conducted in this paper are carried out considering the constraint presented in Equation 1.

2.3. Peripheral beams challenge

One of the most common operating demands for a sensor or EH device is its low mass, so that its dynamics does not influence the behaviour of the original structure. This imposes a constraint to the carriage's mass, thereby limiting the number of beams that can be engaged simultaneously by the carriage, consequently, resulting in a lower number of plectra and lower number of excitations per period. Figure 3 demonstrates this obvious

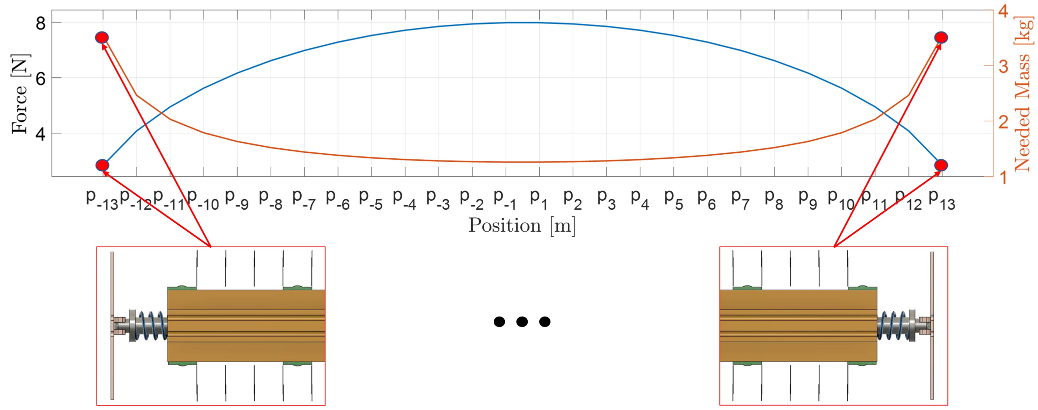

Figure 3: Needed mass to simultaneously pluck the beams and force applied to the beams having selected the needed mass at positions p_{-13} and p_{13}

logic, where the force required to bend a number of beams and the required carriage mass are presented as a function of the device position. As the carriage approaches the position of the beam p_{13}, its acceleration is at its lowest value, which is also true for position p_{-13}, at the device's opposite end. Therefore, the relationship between the acceleration and force necessary to pluck the beams at positions p_{-13} and p_{13} determines the minimum required mass.

Figure 3 shows the response from a 50 mm long device whose design configuration is built based on the aforementioned constraint, having the mass limited to 4 kg, an array of 46 beams, 6 plectra and 4 beams between plectra. Given 2 Hz excitation frequency, the required mass is about 3.5 kg, x :[p_{-13}, p_{13}], which provides a total force of 2.8 N to pluck 6 beams simultaneously. However, the middle-range beams require significantly lower mass to overcome the beams' stiffness as the acceleration of the carriage increases towards the centre of the device. Consequently, once the mass is selected based on positions p_{-13} and p_{13}, the total number of plectra and the number of excitations would be lower than that when the number of plectra is calculated based on the middle beams.

Figure 3 shows that the required mass grows at a higher rate for $p_{\pm(10-13)}$, increasing the difference between the middle values and the peripheral ones, e.g., the required mass increases by 44.0% from $p_{\pm(12)}$ to $p_{\pm(13)}$ while 21.4% from $p_{\pm(11)}$ to $p_{\pm(12)}$. As presented in Figure 4a, the power generated by each beam increases towards the center, e.g., the middle beams generates up to 16

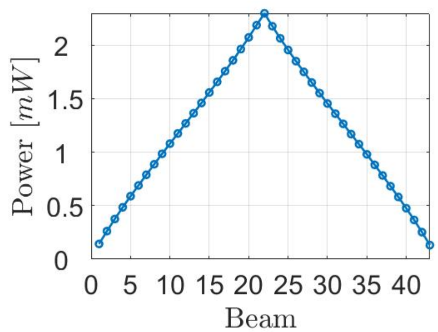

(a)

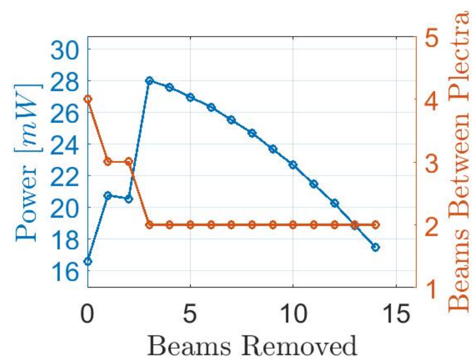

(b)

Figure 4: (a) Average power generated by each beam within the device as the carriage oscillates. (b) Variations in the average power output and number of beams between plectra as peripheral beams are removed from each side.

times more energy than the two most peripheral beams when subjected to a harmonic excitation. Therefore, it may be more advantageous to exclude some of the peripheral beams so that the number of plectra can be increased, as the acceleration increases when the carriage moves towards the middle part of the device. Figure 4b illustrates this behaviour, where the device variations in power output and number of beams between plectra are presented as a function of peripheral beams removed from each side symmetrically. It can be seen that by removing one beam from each side, the power output jumps from 16.6 mW to 20.8 mW, providing 25 % increase.

Next, it is noted that by removing 2 beams from each side, there is a slight decrease in the power output. This can be explained by looking at the red line, which remained the same when one additional beam was removed. As the number of beams between plectra from each side is reduced from 4 to 2, the power output is further increased by 34.6 %, representing a total of 68.7% increase from the original configuration. Figure 4b also shows that further removing beams does not improve the power output as the number of beams between plectra remains constant. Eventually, keep removing the beams allows the number of beams between plectra to decrease to its minimum (1 beam between 2 plectra), however, it does not guarantee that the power output will increase, or achieves its global maximum value. This indicates a balance between removing the beams and decreasing the number of beams between plectra. When a beam is within a region of higher number of excitation, as shown in Figure 4a, it may not be advantageous to decrease the number of beams between plectra. Thus, the number of beams to be removed should be decided by the optimisation algorithm based on the overall power output.

2.4. Optimisation Algorithm

The optimisation algorithm is built based on the relationship between the parameters that constitutes the harvester. They define the device behavior and determine its efficiency based on the parameters, classified as constants, variables, and constraints, presented in Table A.6. The constants are values defined prior to the optimisation process, e.g., the mechanical and electrical properties of the beams that remain unchanged during the optimisation. The variables are the parameters which are determined during the optimisation process and govern the device's performance, e.g., the trade-off between the beam thickness, the tip displacement and the number of beams within the given volume. The constraints are associated to the limits imposed onto the design, e.g., the weight and dimensions of the harvester, and the maximum allowed stress. Appendix A.2 provides more information about the parameters and their classifications related to the harvester's design.

The optimisation objective function is the device's power output $P_T(\mathbf{q}_i)$ over a given time period in the case of a harmonic excitation, otherwise it is an averaged power over some selected time interval. In the case when some experimental data is available, as presented later, the averaging is conducted over the entire record time, $t \in [0, T_R]$. The power is a function of variables and is bounded by constraints, as presented in (2). It should be stressed that the fully coupled electromechanical model of the PE-beam has been constructed and validated earlier in Matlab/Simulink in Machado et al. (2021). The model assumes that all the beams respond at their fundamental natural frequency, which allow modelling each beam as a single-degree-of-freedom system (see Appendix A.1).

The purpose of the optimisation is to maximise the objective function, i.e., the power output, by finding the most appropriate selection of the variables values $\mathbf{q}_i$. This is strongly related to the structure of the first part of the algorithm, which establishes the priorities over the parameters. For example, Equation (A.6) states that the distance between beams is a function of the tip displacement and the thickness of the beams. Therefore, when the beam's thickness t_b is a constant, the power output could be a function of the beam's tip displacement (δ_b) only and $\mathbf{q}_i = \{\delta_b\}$. When it is desirable to optimise the beam's thickness, the power output would be a function of the tip displacement, the substrate thickness (t_s) and/or the piezoelectric thickness (t_p), thus the set of optimisation parameters will be $\mathbf{q}_i = \{\delta_b, t_p, t_s\}$. The algorithm (Yurchenko et al., 2022) is built in a way to adjust for an arbitrary number of optimisation key parameters, depending on the analysis goal. Thus, the following optimisation problem is addressed:

$$\begin{aligned} &\max_{\mathbf{q}_i} P_T(\boldsymbol{q_i}),\ b_{li} \leq \mathbf{q}_i \leq b_{ui}, \\ &P_T(\mathbf{q}_i) = \frac{1}{T} \sum_{j=1}^{n_b} E_j(\mathbf{q}_i), \end{aligned} \tag{2}$$

where $E_j(\mathbf{q}_i)$ is the energy delivered by each beam, b_{li} and b_{ui} are the lower and upper bounds of the i^{th} parameter $\mathbf{q}_i$.

The evaluation of the objective function is performed using the surrogate optimisation algorithm provided by the MATLAB optimisation toolbox. The surrogate algorithm approximates the original problem by another function, i.e, it builds a surrogate surface and iteratively improves it by adding test points, leading to the global maximum values of the objective function. This approach is computationally efficient since it works with the surrogate algorithm, does not require many test points, does not rely on a gradient - which reducing the odds of falling into a local minimum - and is suitable for multidimensional constraint optimisation, as considered in this case.

3. Benchmark response to harmonic excitation

3.1. Optimised response with a prescribed number of beams

To understand the device's power output under various excitation levels three device's configurations of $L_d = 50$ mm, $L_d = 100$ mm and $L_d = 200$ mm will be studied. A rather wide range of excitation frequencies will also be taken, inluding 2 Hz, 5 Hz, 10 Hz, 25 Hz, 50 Hz and 75 Hz. The device optimisation is separately conducted for each excitation frequency to understand the device's parametric dependence. The outcome of the optimisation procedure individually applied to each case is presented in Table 1.

The first column in Table 1 indicates the excitation frequencies f under which the optimisation was carried out for each device's length L_d, presented in the second column. The third column indicates the optimal carriage mass M_{opt} needed for the device to operate at the selected frequency and length. Note that a mass restriction of 4 kg was imposed as a constraint during

Table 1: Device configuration given parameters obtained via surrogate optimization under harmonic excitation.

		Device Configuration									
f	L_d	M_{opt}	l_{M-opt}	t_{s-opt}	δ_b	n_b	n_p	n_{bbp}	n_{ex}	P	Σ
Hz	mm	kg	mm	μm	μm	–	–	–	–	mW	–
	50	3.512	22.08	547	198	49	8	3	224	17.5	0.89
2	100	3.872	48.57	531	200	100	13	4	676	47.5	0.87
	200	3.872	97.54	550	198	198	17	6	1734	121.7	0.89
	50	3.911	24.66	886	143	40	20	1	420	82.6	1.00
5	100	3.956	50.12	701	176	89	45	1	2025	192.2	0.99
	200	3.715	98.95	880	141	163	41	2	3403	412.9	0.97
	50	1.386	25.64	959	132	39	20	1	400	114.8	0.99
10	100	1.667	49.90	906	141	80	40	1	1640	267.9	1.00
	200	2.723	100.63	967	132	155	78	1	6084	633.6	0.99
	50	0.211	25.58	956	132	39	20	1	400	152.0	0.98
25	100	0.291	49.88	1000	126	76	38	1	1482	360.9	0.96
	200	0.216	98.62	1000	128	152	38	2	2964	736.5	0.99
	50	0.053	24.93	1000	126	38	19	1	380	188.2	0.98
50	100	0.039	48.68	1000	128	76	19	2	760	319.7	1.00
	200	0.026	95.97	998	128	152	19	4	1520	779.9	1.00
	50	0.011	23.72	908	140	40	10	2	220	181.3	1.00
75	100	0.012	48.68	1000	128	76	13	3	520	401.1	1.00
	200	0.006	95.51	1000	124	152	13	6	1040	755.2	0.97
	50	0.009	24.99	1000	128	38	10	2	200	197.6	1.00
90	100	0.006	48.67	999	128	76	10	4	400	396.9	1.00
	200	0.004	92.72	987	129	153	11	7	913	803.2	1.00

the optimisation, limiting the overall weight of the device. The fourth column presents the length of the moving mass l_{M-opt} with the plectra. The length of the carriage mass is a function of the number of plectra and the distance between them. The fifth and sixth columns present the optimal beam's substrate thickness t_{s-opt} and the beam's tip displacement δ_b, respectively. There is a trade-off relationship between these two parameters governed by the maximum stress allowed, which is imposed as a constraint in the optimisation procedure, as shown in (A.9). The stress experienced by the beam is given by σ and the ratio between the experienced and the maximum allowed stress is given by $\Sigma = \sigma/\sigma_{max}$.

The number of beams n_b in the device, shown in column seven, is a function of the thickness of the beam, the displacement applied to it and the length of the device (L_d), which informs how many beams can fit within the given volume of the host structure. In column eight, the number of plectra n_p is given, which, to have the highest number of excitations possible, must be half of the number of beams, i.e. $n_b/2$, according to (A.4), implying that the distance between two plectra is equal to the distance between two beams. However, there are two limitations to this rule. The first is related to the carriage mass, i.e., the higher the number of plectra, the higher the mass required to pluck the beams simultaneously. Since the mass is limited, the number of plectra may be reduced to comply with the plucking requirements by increasing the number of beams between plectra n_{bbp}. The second limitation is related to the frequency of the excitation, observed in Figure 2 and addressed in Section 2.2.

The limitation regarding the plucking frequency can be better understood by also looking at the number of beams between plectra in column nine of the table. At 2 Hz, $n_{bbp} > 1$ for all the cases, which is clearly caused by the mass limitation since M_{opt} is around its maximum permitted value of 4 kg. When the frequency is increased to 5 Hz, there is enough energy in the system to allow a higher number of plectra in the device and, therefore, the number of plectra is optimal for the 50 mm and 100 mm configurations, i.e. $n_{bbp} = 1$, while the number of plectra in the 200 mm configuration is still limited by the mass. At 10 Hz, all length configurations are at their best case scenario when it comes to the number of plectra and $n_{bbp} = 1$. The energy in the system is such that a significant drop in the needed mass is observed. As the frequency increases further from 25 Hz to 90 Hz, the required mass decreases, which is reasonable as the carriage acceleration increases. However, the number of beams between plectra increases, decreasing the number of plectra, resulting in a counter-intuitive response of the algorithm, since the tendency observed from 2 Hz to 10 Hz is that the number of beams between plectra tends to reach one as the frequency increases. The reason behind it is that the maximum allowed mass is no longer the limitation but the frequency at which the beams are plucked have increased to a level that it is necessary to remove some plectra in order to ensure that the beams will oscillate for at least half of their vibration period. This is achieved by increasing the number of beams between plectra, thereby changing the pattern of n_{bbp}.

The resultant number of excitations within a half-period presented in column ten (see Appendix A.3), demonstrates quadratic dependence on the

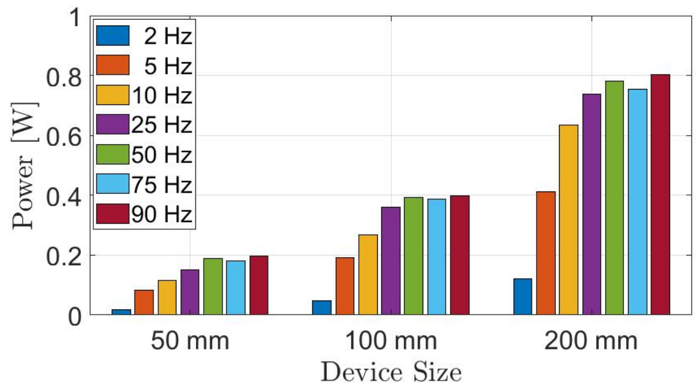

Figure 5: Power output under varying excitation frequency as presented in Table 1.

number of beams. Column eleven presents the average power output of the device while column twelve presents the stress ratio experienced by each beam at their fixed end (all beams are identical and subjected to the same displacement). The device performance improves at higher frequencies up to a certain level. Note that there is a consistent power increase up to 50 Hz. At 75 Hz, however, the 50 mm and 200 mm configurations experience a drop from 188.2 mW to 181 mW, from 779.9 mW to 755.2 mW, respectively. Note also that the algorithm has given a preference to higher displacements rather than thicker beams at the lower frequencies range (2-5 Hz). Conversely, at the higher frequencies (10-90 Hz) one may observe the opposite optimisation trend with relatively low optimal displacement and relatively high beam's thickness.

For a better visualization of the relationship between the excitation frequency and the power outputs, the results from Table 1 are also depicted in Figure 5 and combined based on the device's length. Figure 5 presents the optimised performance of the these configurations as a function of the excitation frequency. The average power output clearly reaches a saturation with the increase of the excitation frequency, implying that higher excitation frequency will not bring any further increase in the power output. Moreover, it can be seen that the power output of the device has a nonlinear dependence with respect to its length, meaning that a single 100 mm long device will generate more power than two 50 mm devices, as well as a single 200 mm device will produce more power than two 100 mm devices. This is related to the relationship between the total number of excitation and the number

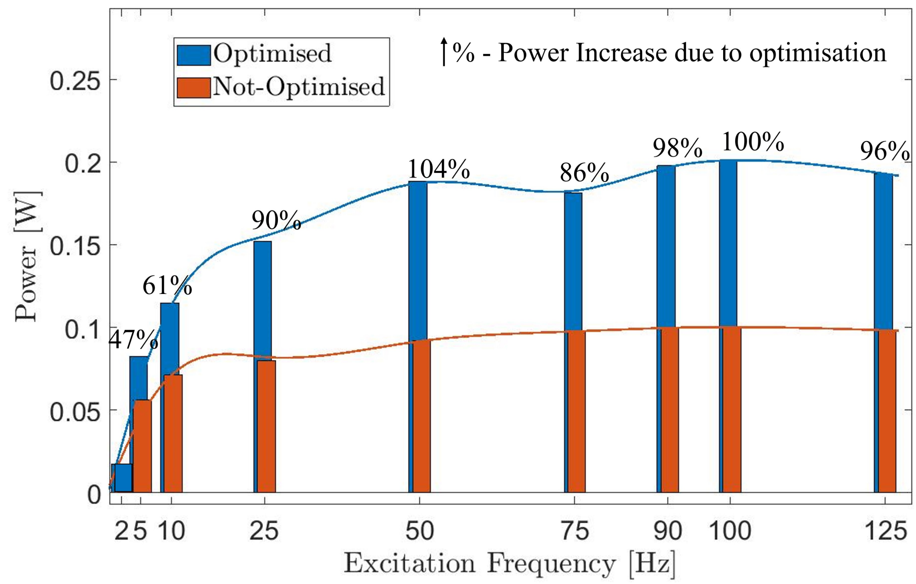

Figure 6: Output power under varying excitation frequency for the 50 mm long device optimised at 2 Hz only (red) and the former optimised at each selected frequency (blue).

of beams. It should be stressed that this difference becomes negligible when the saturation is reached, i.e., at high excitation frequencies.

It seems obvious to ask whether each configuration should be optimised to a particular excitation frequency or optimising it a specified frequency is enough for optimal operation at other frequencies. To answer that, Figure 6 presents the power output of the 50 mm long device excited harmonically by different excitation frequencies. Two sets of results - without (red) and with optimisation (blue) - are presented. Namely, the data presented in red has been generated by the 50 mm long device whose parameters have been optimised at 2 Hz, therefore the first bar at 2 Hz is shown in blue. Then, having fixed this set of parameters, this device was subjected to other excitation frequencies, presented in the chart. The second set of results, shown in blue, was obtained by individually tuning the device's parameters to the targeted excitation frequency through the optimisation process. Each set of bars in Figure 6 is accompanied by its respective increase in percents, indicating the impact of the optimisation procedure in the design process. At 5 Hz the optimised device was able to deliver 47% higher power output than its non-optimised counterpart. The rise in power output becomes more prominent at higher frequencies, reaching up to 104% at 50 Hz. The shape of both data sets, however, show a similar tendency towards saturation, from which further increase in excitation frequency does not bring any substantial power increase. The excitation frequency saturation limit is related to the natural frequency of the beam due to the reasons explained in Section 2.2 and exemplified in Figure 2.

3.2. Optimisation with peripheral beams extraction

It has been demonstrated that it may be beneficial to extract some of the peripheral beams so that the number of plectra can be increased when it has been limited by the maximum allowed carriage mass. Since the acceleration is very small at the sides of the device, the peripheral beams removal will increase the number of plectra based on the carriage. Consequently, the device's performance can be improved, since a higher number of excitations per period will be achieved. Two approaches are analysed to determine the influence of the peripheral beam extraction. The first approach uses the optimisation procedure by adding the parameter that controls the empty slots at the peripheral areas of the device. The second approach makes use of the results presented in Table 1 and conducts a sweep analysis removing beam by beam from each end symmetrically until the best scenario is reached, as illustrated in Figure 4b. Therefore, the first approach adds one more parameter to the optimisation process making it computationally more expensive. In this case, the beam is not extracted based on an established configuration, but the algorithm informs the number of beams' slots that should be empty. The parameter that provides this information is denoted as $n_s^{\varnothing}$ and the remaining number of beams is denoted by $\bar{n}_b$.

Table 2 presents the results of the optimisation having added the parameter $n_s^{\varnothing}$, which the objective function now directly depends on. The same length configurations were studied under excitation frequencies ranging from 2 Hz to 50 Hz. The results show that the benefit of having considered the $n_s^{\varnothing}$ parameter is more significant at 2 Hz, where the number of beams between plectra is considerably reduced (from 3 to 1) for the 50 mm configuration, whereas in other configurations the number of plectra was reduced twice. This reduction had a substantial impact on the power output, allowing the device to increase its performance in 72%, 51%, and 82% for the 50 mm, 100 mm and 200 mm configurations, respectively. Another benefit from this approach is noticed in the reduction of the beams' number, having a direct impact on the device's cost. Note that the number of beams dropped from

49 to 35, from 100 to 62, and from 198 to 125 for the 50 mm, 100 mm and 200 mm configurations respectively when excited at 2 Hz.

As the operation frequency rises, so decreases the gain from increasing the distance between the peripheral beams and the sides of the device. At 5 Hz, for example, the number of beams between plectra for the 50 and 100 mm configuration is already 1, as shown in Table 1, therefore it is expected that the optimisation with the extra $n_s^{\varnothing}$ parameter does not lead to a significant impact as it did at 2 Hz. Table 2 indicates 0.2% increase for the 50 mm configuration, however the device is now considerably lighter, having its mass dropped to 59% of the original mass. The 100 mm device configuration excited at 5 Hz is an interesting case, where, even though there was no space to improve n_{bbp} parameter, the optimisation informs of a configuration with power output 14% higher than the configuration presented in Table 1. The reason is that there was an alternative configuration, which required $n_s^{\varnothing} = 3$ to be a feasible option. Therefore, the parameter $n_s^{\varnothing}$ not only reduces the number of beams between plectra but also widen the range of possible parameter combinations. In the case of 200 mm device excited at 5 Hz, the number of beams between plectra was reduced from 2 to 1, which allowed increasing the power output by about 22%. It is shown that at 5 Hz the performance improvement due to the addition of $n_s^{\varnothing}$ parameter is considerably lower than that at 2 Hz. This pattern is followed when the excitation frequency is further increased to 10 Hz. Table 2 indicates that there is absolutely no gain in considering this approach at higher frequencies. Note, however, that the

Table 2: Device configuration given parameters obtained via surrogate optimization under harmonic excitation with peripheral beams removal.

Device Configuration												
f	L_d	M_{opt}	l_{M-opt}	t_{s-opt}	δ_b	$\bar{n}_b$	n_p	n_{bbp}	n_{ex}	P	P_{Table1}	$n_s^{\varnothing}$
Hz	mm	kg	mm	μm	μm	–	–	–	–	mW	mW	–
2	50	3.889	24.42	517	200	35	25	1	275	30.2	17.5	16
	100	3.959	49.99	772	139	62	23	2	414	71.9	47.5	28
	200	3.629	99.39	862	145	125	28	3	1232	221.5	121.7	40
5	50	2.951	25.61	878	141	37	21	1	357	82.8	82.6	2
	100	3.471	50.63	936	135	73	40	1	1360	219.3	192.2	3
	200	2.554	100	890	142	146	81	1	5346	502.9	412.9	16
10	50	1.266	24.88	1000	125	38	19	1	380	109.9	114.8	0
	100	1.081	50.56	930	137	77	40	1	1520	266.7	267.9	2
	200	2.654	99.91	1000	127	152	76	1	5852	625.0	633.6	0

outputs of the 50 mm, 100 mm, and 200 mm configurations at 10 Hz present some discrepancies in the set of optimal parameters when compared to Table 1. One would expect the algorithm to yield the previous solution once no beams needed to be removed. However, it also needs to be considered that the same number of function evaluations were carried out for the objective functions with two and three parameters, which explains the slight discrepancy. However, this difference is negligible and, thus, does not require further function evaluations.

The second approach considers the results from the original optimisation with two parameters (the tip displacement and the substrate thickness) and conducts a sweep analysis to study the effects of removing peripheral beams from their slots, having a lower computational cost. Thus, from Table 1 it can be concluded that the configurations suspected to be improved by this process are 50 mm, 100 mm, and 200 mm at 2 Hz, and 200 mm at 5 Hz, as their number of beams between plectra are higher than one due to mass limitation. Figure 7 shows the results of the sweep analysis, where the left axis presents the power output and the right axis presents the number of beams between plectra as a function of the number of extracted beams. Figure 7a presents the response of 50 mm configuration at 2 Hz. The power output increases from 17.5 to 23.5 mW, reaching a 34.3% growth after removing two beams from each side of the device, which drops n_{bbp} from three to two. As more beams are being removed, the power output drops while the number of beams between plectra remains the same. After removing twelve beams from each side, there is another sudden rise in power output, which takes it to 25.9 mW, bringing a total of 48% increase from the device with totally 24 beams removed. A similar behaviour is observed with 100 mm configuration at 2 Hz presented in Figure 7b. However, the removal of just a single beam at each side leads to power increase of about 20%. When two more beams are removed, the power output increases about 50.9%. However, further beams removals leads to decreasing power output while the number of beams between plectra remains the same. When 23 beams are removed from each side, the parameter n_{bbp} reaches unity and the power output rises to 71.9 mW, representing 51.5% power increase.

Figure 7c presents the response of 200 mm device at 2 Hz, where the removal of 3 beams at each side takes the power output from 121.7 mW to 176.3 mW. Further removal of 5 beams from each side delivers 207.6 mW, resulting in an overall 70.6% power increase compared to its original configuration, with 2 beams between plectra. Contrary to the pattern observed in

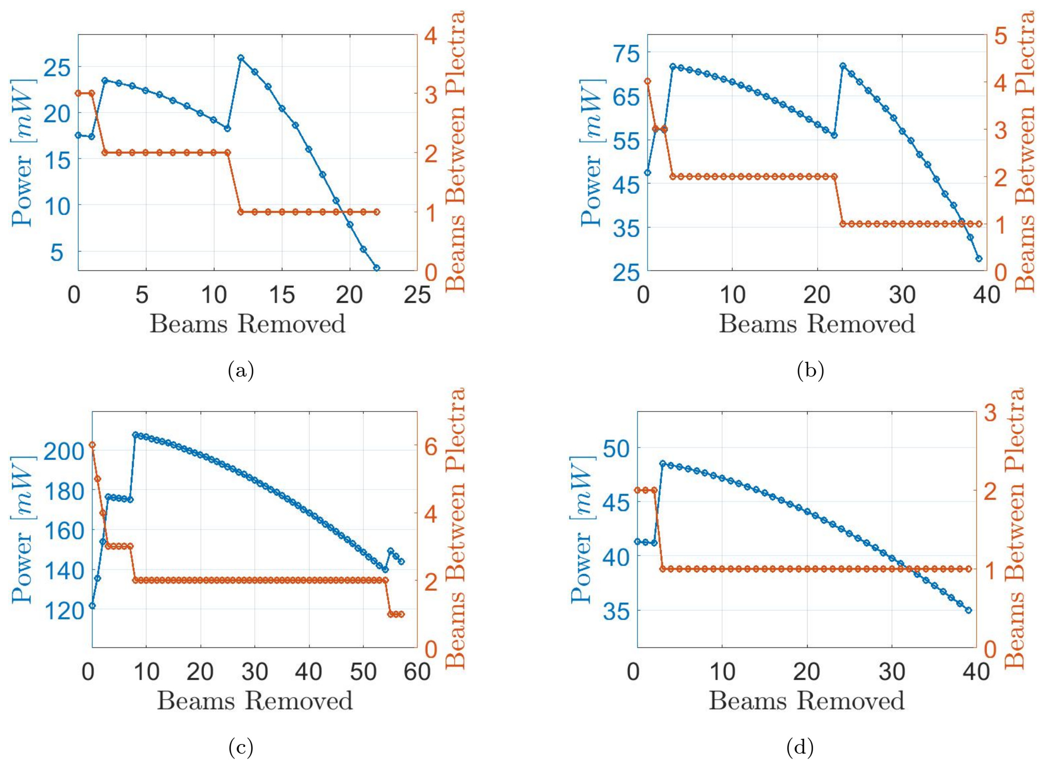

Figure 7: Influence of removing peripheral beams from their slots: (a) 50 mm at 2 Hz; (b) 100 mm at 2 Hz; (c) 200 mm at 2 Hz; (d) 200 mm at 5 Hz.

50 mm and 100 mm configurations, further beam removal leading to $n_{bbp} = 1$ does not lead to improved power output. The last case observed with this approach is the 200 mm configuration excited at 5 Hz, presented in Figure 7d. Here, the removal of 3 beams from each side is enough to decrease the number of beams between plectra from 2 to 1 and increase the power output from 412.9 mW to 484.8 mW demonstrating 17% rise. This result corroborates the conclusion that at higher excitation frequencies the beam removal poses little influence on the device's performance.

The optimisation approach is clearly superior to the process of removing the beams one by one. When the optimisation is used, the removal of beams gives place to other parameter combinations, thus the likelihood of higher power generation is increased. The optimisation approach yielded 16.6%, 6.7%, and 3.7% more power for 50 and 200 mm configuration excited at 2 Hz, and the 200 mm excited at 5 Hz, respectively. Both approaches yielded the same power output for 100 mm configuration excited at 2 Hz. This result is congruent with the expected behaviour of the algorithm, i.e., it must yield at least the same power output as the non-optimised approach. Therefore, introducing $n_s^{\varnothing}$ parameter to the algorithm is beneficial when the mass limitation is imposed, as it allows increasing the number of plectra and decreasing the number of beams between plectra.

4. Optimisation of the device under narrow-band excitation

4.1. Computational considerations

Since ambient vibrations are often not purely harmonic, it is critical to assess the performance of the device under a narrow band excitation as it may change the harvester's optimal set of parameters. The inhomogenuity of the excitation input can be modelled by inducing random variations of the excitation frequency causing a disorder in the excitation. It assumed that the phenomena involved may be treated as a weakly stationary stochastic process, therefore the excitation is modelled as a harmonic function with a white noise phase modulation (Dimentberg et al., 1995), and can be written as:

$$\mathbf{x}(\mathbf{t}) = \lambda \sin \mathbf{v}(t), \quad \frac{d}{dt}\mathbf{v}(t) = \nu + \gamma\xi(t),\ D = \gamma^2 \tag{3}$$

where $x(t)$ is the excitation, $\xi(t)$ is a zero mean Gaussian white noise, ν is the mean excitation frequency and D is the noise intensity.

In addition to the excitation amplitude, it's important to account for the noise intensity and the number of periods essential to generate representative input data. In the next set of simulations the noise level was $\gamma = 0.025$ and the mean excitation frequency was 2 Hz, as presented in Figure 8a. Figure 8b presents the power output of each beam within the 50 mm long device after 10, 100 and 1000 seconds of simulations. Longer simulations directly impact the optimization time, however, Figure 8b clearly shows that there is no significant discrepancy between the outcomes of the 10 s, 100 s and 1000 s simulations for 2Hz mean excitation frequency. In fact it is less than 2% between 100 s and 10 s, less than 1% between 1000 s and 100 s. Based on this evidence, the optimisation procedure is carried out for the device subjected to 10 s of this excitation.

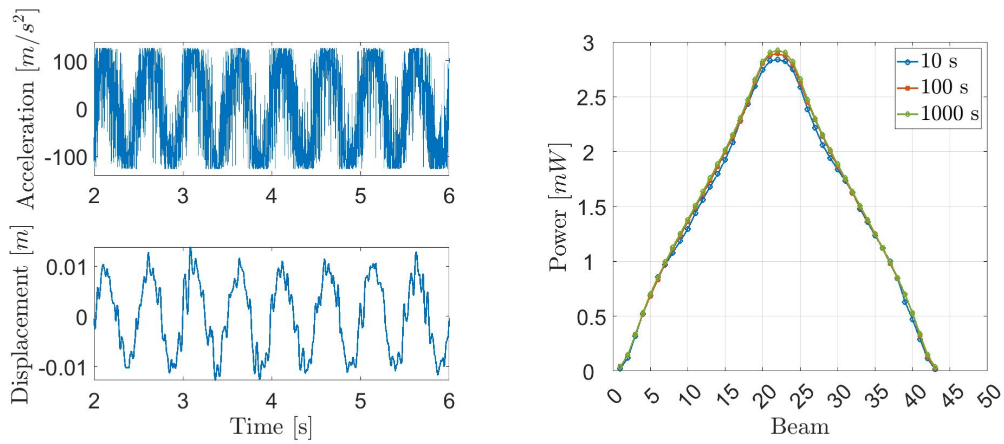

(a) (b)

Figure 8: (a) Excitation input (top - acceleration) and output of the carriage (bottom - displacement) (b) 50 mm long device response under 10 s, 100 s, and 1000 s simulation time.

To illustrate the influence of the narrow band excitation on the device's performance, Figure 9 presents the response of the device under two excitation inputs- with the noise, as in Figure 8a, and a purely sinusoidal signal. The blue graph demonstrates the result of the optimisation procedure based on a purely sinusoidal excitation input. The red graph is obtained by maintaining the same set of parameters, optimised earlier, and adding the noisy input later. In this case an increase of 24% in the total power output can be observed. It was expected since an additional noise pumps some extra energy into the system. Next, the optimisation procedure was applied to the device subjected to the noise with the same intensity level. Thus, the green graph presents the power output generated by the device under the narrow band excitation. The outcome shows a further improvement in the power output, which is not very significant in the total power generated, i.e., $<< 1\%$, although it was able to suggest a device which requires 4 beams to be removed, where the middle beams generate 10% more power compared to the previous configuration.

Therefore, the total power from the optimised and non-optimised devices under the same input with noise indicate that either of them is able to respond at satisfactory similar levels. This is particularly helpful when it comes to computational cost. When the excitation input is purely harmonic, it is fairly simple to predict the device behaviour within a period and perform the calculations related to its performance. This is reflected well in Figure 9, which shows that the power generated by each beam has a linear trend when no noise is present (blue). This implies that a half-period provides enough data to understand the behaviour of the device, which, in turn, allows establishing beforehand how many times each beam is excited and the total power generated at a low computational cost. On the other hand, when noise is present in the excitation input, each beam needs to be individually analysed under a longer time interval, as the real number of excitations of each beam per period is unknown. This is also observed in Figure 9 through the nonlinear trend with a smooth peak transition (red and green) of the power generated by each beam.

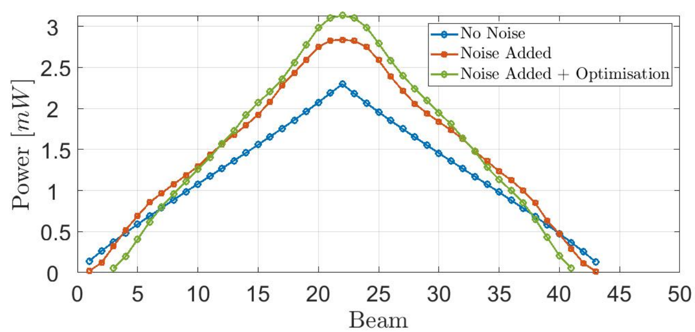

Figure 9: Power generated by each beam within the device under pure harmonic excitation (blue), narrow band phase modulation and no optimisation (red), narrow band phase modulation and optimisation (green).

4.2. Response of the device to the narrow band excitation.

In this section, further analysis is carried out to understand how the classical narrow band excitation impacts the choice of parameters in the optimisation process. The optimisation methodology is applied to the 50 mm, 100 mm, and 200 mm configurations subjected to a mean excitation frequency of $\nu = 2$ Hz and two noise levels of $\gamma_1 = 0.025$ and $\gamma_2 = 0.25$. Figure 10 presents the response of the 50 mm device due to an input acceleration with $\gamma_1 = 0.025\ W$.

Table 3 presents the mean power output $\bar{P}$ of the device along with the parameters related to its construction design. Its last column, P_{Table1}, presents the power output given for the same length configuration as presented in Table 1. According to Table 3, the devices are capable of delivering a higher power output due to the narrow band input signal. The observed increase in power output of the 50 mm, 100 mm, and 200 mm devices are 32.6%, 26.5% and 29.4%, correspondingly when $\gamma = 0.025$. By comparing the results presented in Table 3 against those presented in Table 1 under the same excitation frequency, it becomes clear that the excitation characteristics affect not only the power output but the entire device configuration.

Most of the parameters in Table 3 have experienced significant changes to their values when compared to those in Table 1. For example, even though the same tip displacement is observed in Tables 1 and 3 for the 50 mm configuration, the thickness in Table 3 is 11% higher than the previous case, leading to a beam 38.6% stiffer. Consequently, a lower number of plectra was achieved and more beams between plectra were imposed. In the 100 mm configuration, the beams' thickness experienced a slight decrease of 3.4%. As a result, the alterations in this configuration were mild, as observed in the conservation of n_p and n_{bbp}. In the 200 mm device, the beams' tip displacement is decreased by 4.6% while its thickness increased of 15.8%. This combination resulted in lower number of plectra and higher number of beams between plectra, as was the case for the 50 mm device.

Table 3 also presents the results of an optimisation procedure carried out for the 50 mm device excited with two order of magnitude higher noise intensity level ($\gamma^2 = 0.25^2$). The power output is increased by 41%, however, the parameters were kept the same as in the system excited with a lower noise level. Therefore, the increase in the power output is mostly caused by the rise in energy pumped into the system through noise. It is also important to note that the number of excitations given in Table 3 is not related to the actual excitation input but to the relationship between number of beams, plectra and beams between plectra given for a mean half - period (according

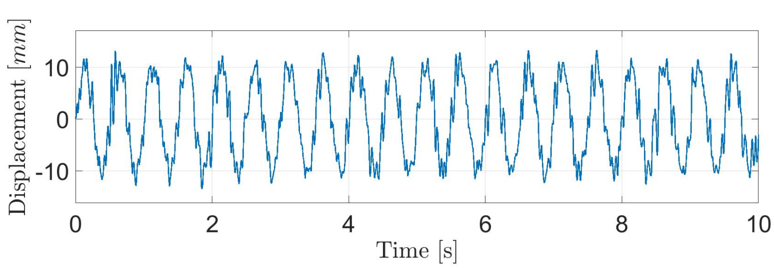

Figure 10: Carriage displacement for the 50 mm device length configuration excited at 2 Hz with a white noise phase modulation with a power level of $\sigma = 0.025\ W$.

Table 3: Device configuration given parameters obtained via surrogate optimization under narrow band excitation.

Device Configuration											
$\gamma_1 = 0.025$											
f	L_d	M_{opt}	l_{M-opt}	t_{s-opt}	δ_b	n_b	n_p	n_{bbp}	n_{ex}	$\bar{P}$	P_{Table1}
Hz	mm	kg	mm	μm	μm	–	–	–	–	mW	mW
	50	3.537	22.46	610	200	46	6	4	156	23.2	17.5
2	100	3.691	47.70	513	200	102	13	4	702	60.1	47.5
	200	3.798	95.78	637	189	185	12	8	1164	157.5	121.7
$\gamma_2 = 0.25$											
2	50	3.544	22.46	610	200	46	6	4	156	32.7	17.5

to (A.4)). Since the power output is higher at a higher noise level, it is clear that the real number of excitations is higher in the latter case.

5. Case study I: Performance of the device attached to an IC engine

Having analysed the devices performance under harmonic and narrow band excitations, in this section the device will be subjected to an experimental excitation data, as if the device were attached to a real vibrating system. The excitation data was collected by a PCB triaxial charge output accelerometer, Model 356A70, with sensitivity of 0.304 $pC/(m/s^2)$ for the x-channel, and with sample rate set to 1 kHz. The accelerometer was placed on an automobile IC engine, as shown in Figure 11a, and the experimental data of 60 s was extracted from the vertical motion of the engine, as shown in Figure 11a.

It is clear from the zoomed-in window that the data is not sinusoidal and presents the characteristics of a bounded noisy signal with rather wide band spectra. Thus, the device will respond at its natural frequency, which can be adjusted through the design and optimisation procedure. Figure 11b presents the response of the harvester to the engine vibrations as the natural frequency of the device is varied. The first three natural frequencies of the mass response are 26.8 Hz, 53.6 Hz and 80.4 Hz. Independently of the size of the device, the average displacement of the carriage mass is a constant for a given natural frequency of the mass-damper-spring system of the harvester as long as the device does not change the dynamics of the engine. This carriage mass of 50 mm device is designed to operate under 23.4 Hz, the

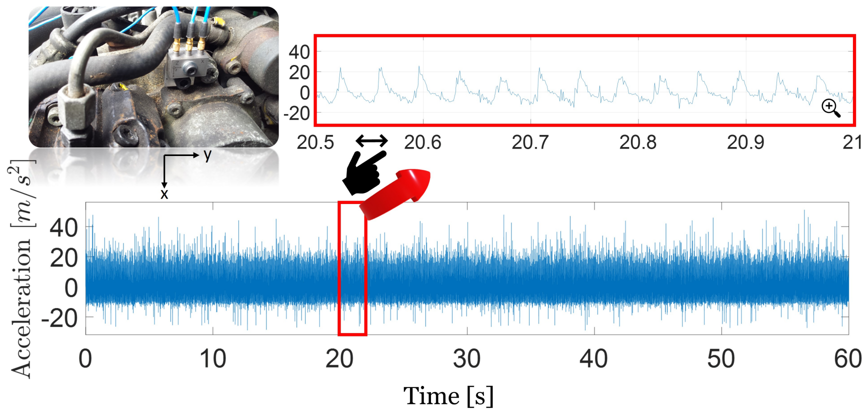

(a)

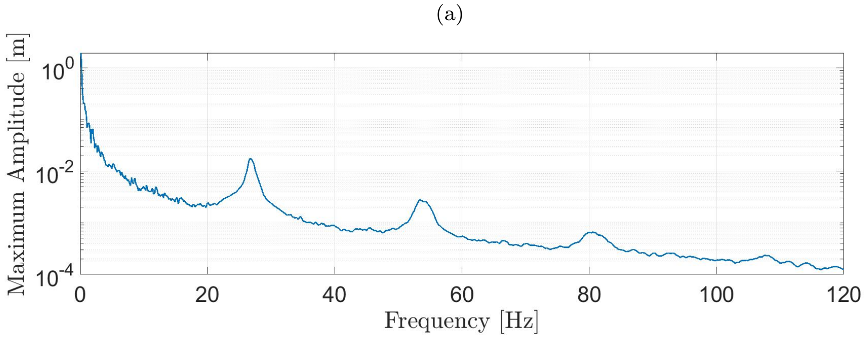

(b)

Figure 11: (a) Accelerometer position and measured acceleration data in the x-axis under a sample rate of 1000 Hz and sample length of 60 secs. (b) Frequency response of the carriage mass given the experimental input presented in Figure 11a.

second peak, which induces appropriate vibration amplitudes, i.e., ranging within $[-(L_d - L_c)/2,\ (L_d - L_c)/2]$.

Table 4 presents the performance of the device designed to operate attached to the IC engine. The solution obtained using the optimisation procedure without beam removal for short (50 mm) and lightweight (0.193 kg) device suggests that it is able to generate 162.6 mW on average. Consequently, this device is capable of autonomously powering several sensors and data transfer unit.

Table 4: Device configuration given parameters obtained via surrogate optimisation having the experimental data of an automobile IC engine as an input.

Device Configuration										
f	L_d	M_{opt}	l_{M-opt}	t_{s-opt}	δ_b	n_b	n_p	n_{bbp}	n_{ex}	P
Hz	mm	kg	mm	μm	μm	–	–	–	–	mW
23.4	50	0.193	25.60	955	132	39	20	1	400	162.6

6. Case study II: Device placed inside wind turbine blades

This section presents the capability of the proposed device to power a wireless accelerometer. Such accelerometer can be used for vibration-based structural health monitoring of wind turbine blades. Structural health monitoring is potentially a major field of application for energy harvester devices, which comes from the great potential of harvesters to provide autonomous operation of sensors located in the areas of difficult access. Several designs have been proposed using various transduction mechanisms, e.g., Joyce et al. (2014) presented an electromagnetic harvester able to generate 3.3 mW when operated at 44 RPM. However, at lower speeds, the power output was significantly lower, whereas at higher speeds the centrifugal effect restrained the displacement of the magnet. Zhang et al. (2020) present a vibro-impact dielectric elastomer generator, which was implemented into a turbine's hub. The maximum power generated was 0.71 mW, yielded when the turbine operates at 3.99 ms^{-1}. Similarly to the previous design, at higher rotating speeds the centrifugal force restrained the displacement of the inner ball that impacted the two dielectric elastomer membranes covering the sides of the device.

In this paper, it's proposed to use the vibration caused by the flapwise and edgewise motion of the blades. Therefore, the analysis is conducted considering the measurements from a sensor located 40.2 m from the hub of a 85 m long blade of a generic simulated 10 mW wind turbine. Typically, such blades have relatively large internal space to place a thin long device along the favorable direction. The data related the edgewise and flapwise motions of the blades are used as the excitation input for the device. The illustration indicating the position of the sensor as well as the edgewise and flapwise motions of the blades is presented in Figure 12. The harvester is positioned at an angle θ_{avg} which represents the average angle between the

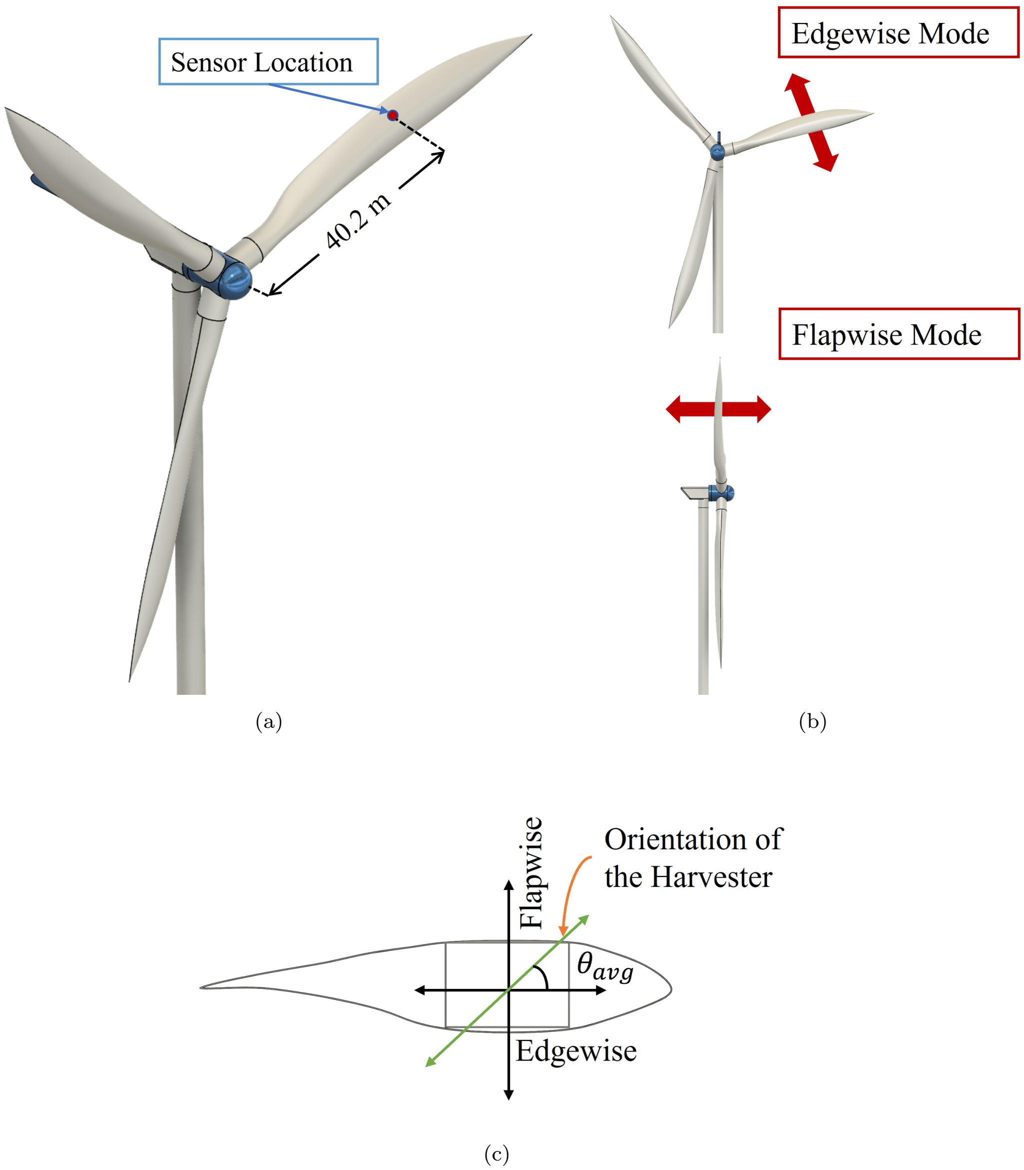

Figure 12: (a) Sensor location of the blade of the wind turbine. (b) Blade motion: edgewise (top) and flapwise (bottom). (c) Orientation of the harvester.

edgewise and flapwise motions, as presented in Equation (4).

$$\theta_{avg} = \frac{\Sigma_{i=1}^{n} \arctan\left(\frac{a_i^{flap}}{a_i^{edge}}\right)}{n}, \tag{4}$$

where a_i^{flap} and a_i^{edge} are the acceleration amplitudes of the flapwise and edgewise motion of the blade, respectively, and n is the number of data samples. At this angle, a higher displacement amplitude is obtained, which facilitates the acceleration of the carriage as it plucks the beams. The resultant acceleration a_r is calculated as presented in Equation (5):

$$a_r = a_i^{edge} \cos(\theta_{avg}) + a_i^{flap} \sin(\theta_{avg}), \tag{5}$$

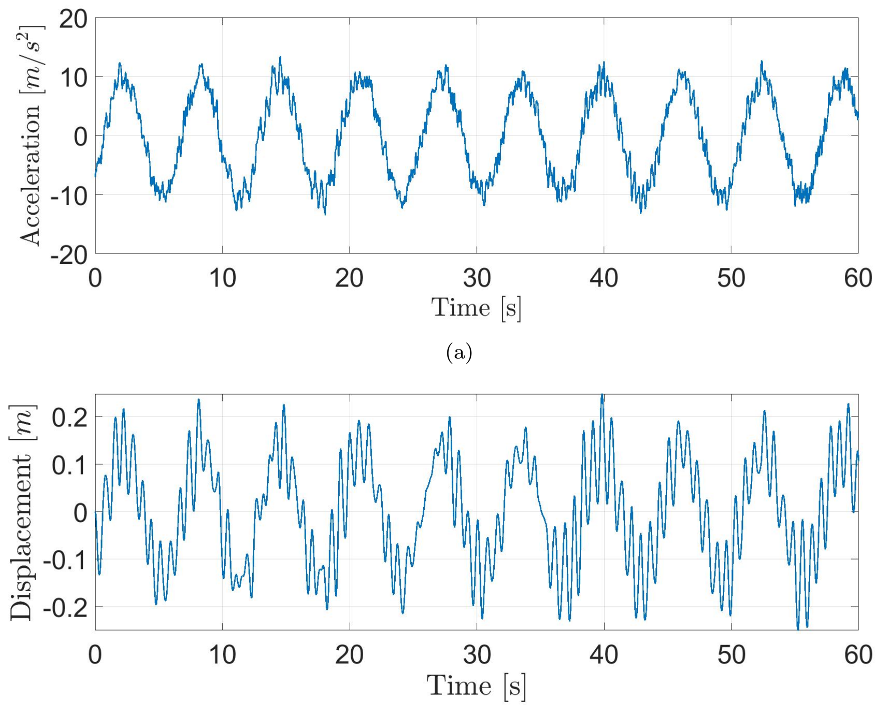

(a)

(b)

Figure 13: (a) Blade vibration obtained via simulation, (b) carriage response to blade vibration data when device's natural frequency is 1.36 Hz.

As presented in Figure 13a, the wind conditions considered impose a 9.6 RPM speed to the rotor of the turbine. The optimisation is conducted

Table 5: Device configuration given parameters obtained via surrogate optimization having the turbine data as an input.

Device Configuration											
f	L_d	M_{opt}	l_{M-opt}	t_{s-opt}	δ_b	n_b	n_p	n_{bbp}	n_{ex}	P	$n_s^{\varnothing}$
Hz	mm	kg	mm	μm	μm	–	–	–	–	mW	–
0.16	1000	49.23	493.22	387	200	1014	84	7	36372	291.2	166

considering a 60 s acceleration data sample, or 9.6 cycles, from one of the blades. Figure 13b shows the displacement response of the carriage to the acceleration imposed. The mean excitation frequency is 0.16 Hz, which is considerably low and limits the performance of the proposed device. Note that the accelerometer has several modes of operation which require different amounts of operation power. In the current scenario, there are two main stages: first, 5 min long data acquisition requires a constant supply of 144 mW. Second, 2 min data transmission requires a constant supply of 288 mW. Therefore, that cycle lasts 7 min in total and is repeated up to 20 times per day. The first stage demands 43.2 J while the second stage demands 34.56 J per cycle, thus the total energy required within a day is about 1.56 kJ. Therefore, to meet the above demands the harvester has to generate at least 180 mW on average, assuming no losses.

To ensure the most effective vibration energy harvesting, the harvester should be placed within the blades at $\theta_{avg} = 80.7°$. As presented in Figure 5, the two simplest ways to increase the device power output is by increasing the operating frequency and increasing the device length. Since the operating frequency is pre-established, the length of the device can be adjusted to meet the powering requirements of the application. Clearly, the length and weight of the carriage are limited by the host structure, thus a 1.0 m device of 50 kg is used due to very low excitation frequency. It exerts a maximum force of 25 N at the highest acceleration point of the period. This configuration is subjected to the optimisation routine, yielding the parameters for best performance, as presented in Table 5. From Table 5 one can observe that the device is capable of generating 291.2 mW, delivering the required average power to the monitoring sensor.

Conclusion

Design processes are continuously evolving and demand advanced prescriptive analytical tools to assist in goal-oriented decisions. In this study, it has been presented the importance of applying such tools in energy harvesting design through an optimisation technique that takes into account constraints from real operating conditions. Data is gathered as a response to changes in leading parameters. That generates traits which are essential to establish a surrogate model to investigate the design space. Adopting this approach allows the creation of several designs in a fraction of the time it would take to create it via traditional optimisation methods. Each candidate design is assessed against others for best performance. This is repeated within a given time analysing the design space and producing data, which is later surveyed to establish relationships between inputs and outputs. The best parameters combination is then selected based on their best performance.

The optimisation process is conducted for four excitation scenarios, two of which are purely analytical: harmonic, and narrow band - harmonic function with a white noise phase modulation. The other two analyses were conducted for two scenarios considered: the experimental data collected from an automobile IC engine and the numerical data from FEM simulation of out-of-plane oscillations of wind turbine blades. Three length configurations were analysed for performance under analytical excitations: 50 mm, 100 mm, and 200 mm. At lower frequencies ($f < 25\ Hz$), their performance exceeds the length proportionality (up to 271 %) indicating that it is better to have one 100 mm long than two 50 mm long devices and/or one 200 mm long than two 100 mm long. However, this tendency will settle at higher frequencies to the proportionality of the length increase. Several excitation frequencies were considered to understand their effects onto the device's performance. Optimisation procedure applied to specific operating frequency conditions proved to be vital, doubling the power output in some cases. Next, the effect of removing peripheral beams was studied. The peripheral beams were limiting the number of plectra allowed, since, at their positions, the carriage acceleration was small at low frequencies. Consequently, the plectra were incapable of overcoming the beams' resistance caused by their total stiffness. Having added the peripheral beams removal parameter to the optimisation algorithm, the power output increased up to 82%. This has demonstrated a great versatility of the developed algorithm and the device ability to tune to various excitation conditions.

In the two case studies, the input amplitudes were predefined allowing limited excitation displacement. Consequently, the excitation amplitude was matched to that of the desired length of the device via adjustment of the natural frequency of the mass-spring-damper system of the harvester. In the first case scenario, the generated solution was 50 mm long, weighted 0.193 kg, and generated 162 mW. Given its dimensions and lightweight, it can be easily attached to the engine to power a sensor and/or a data transfer unit. In the second case scenario, the solution provided meets the powering requirements of a sensor equipment applied to monitor 85 m long wind turbines blades. In this application, the device obtained was 1 m long, weighted 49.23 kg and was able to generate 291 mW. In all cases, it has been demonstrated the impact of the optimisation procedure in the performance of energy harvesters and how this area can be explored to meet the demands of industry.

Acknowledgements

The authors would like to acknowledge and are thankful for the support received from the Brazilian National Council for Scientific and Technological Development—CNPq, grant 202615/2019-7. The authors would also like to acknowledge and thank Anders Melchior Hansen for providing the vibration data of the wind turbine blade.

References

Ali, F., Raza, W., Li, X., Gul, H., Kim, K.H., 2019. Piezoelectric energy harvesters for biomedical applications. Nano Energy 57, 879–902.

Alrashdan, M.H., 2020. Mems piezoelectric micro power harvester physical parameter optimization, simulation, and fabrication for extremely low frequency and low vibration level applications. Microelectronics Journal 104, 104894.

Bao, B., Wang, Q., 2021. A rain energy harvester using a self-release tank. Mechanical Systems and Signal Processing 147, 107099.

Cai, W., Harne, R.L., 2019. Vibration energy harvesters with optimized geometry, design, and nonlinearity for robust direct current power delivery. Smart Materials and Structures 28, 075040. doi:10.1088/1361-665x/ab2549.

Cao, Z., Ma, H., Yu, X., Shi, J., Yang, H., Tan, Y., Ren, G., 2022. Global dynamics of a vibro-impact energy harvester. Mathematics 10. doi:10.3390/math10030472.

Covaci, C., Gontean, A., 2020. Piezoelectric energy harvesting solutions: A review. Sensors 20. doi:10.3390/s20123512.

Daraji, A.H., Hale, J.M., Ye, J., 2021. Optimisation of energy harvesting for stiffened composite shells with application to the aircraft wing at structural flight frequency. Thin-Walled Structures 161, 107392.

Dimentberg, M.F., Hou, Z., Noori, M., 1995. Stability of an sdof system under periodic parametric excitation with a white noise phase modulation. CRC Press Mathematical Modelling Series .

Fang, S., Zhou, S., Yurchenko, D., Yang, T., Liao, W.H., 2022. Multistability phenomenon in signal processing, energy harvesting, composite structures, and metamaterials: A review. Mechanical Systems and Signal Processing 166, 108419.

Fu, H., Mei, X., Yurchenko, D., Zhou, S., Theodossiades, S., Nakano, K., Yeatman, E.M., 2021. Rotational energy harvesting for self-powered sensing. Joule 5, 1074–1118. doi:https://doi.org/10.1016/j.joule.2021.03.006.

Fu, H., Yeatman, E.M., 2017. A methodology for low-speed broadband rotational energy harvesting using piezoelectric transduction and frequency up-conversion. Energy 125, 152–161. doi:https://doi.org/10.1016/j.energy.2017.02.115.

Gorlatova, M., Sarik, J., Grebla, G., Cong, M., Kymissis, I., Zussman, G., 2014. Movers and shakers: Kinetic energy harvesting for the internet of things. SIGMETRICS Perform. Eval. Rev. 42, 407–419.

Hashim, A.A., Mahmoud, K.I., Ridha, H.M., 2021. Geometry and shape optimization of piezoelectric cantilever energy harvester using comsol multiphysics software. International Review of Applied Sciences and Engineering 12, 103 – 110. doi:10.1556/1848.2021.00170.

Izadgoshasb, I., Lim, Y.Y., Tang, L., Padilla, R.V., Tang, Z.S., Sedighi, M., 2019. Improving efficiency of piezoelectric based energy harvesting from human motions using double pendulum system. Energy Conversion and Management 184, 559–570. doi:https://doi.org/10.1016/j.enconman.2019.02.001.

Joyce, B.S., Farmer, J., Inman, D.J., 2014. Electromagnetic energy harvester for monitoring wind turbine blades. Wind Energy 17, 869–876. doi:https://doi.org/10.1002/we.1602.

Kim, H.S., Kim, J.H., Kim, J., 2011. A review of piezoelectric energy harvesting based on vibration. International Journal of Precision Engineering and Manufacturing 12, 1129–1141. doi:10.1007/s12541-011-0151-3.

Lee, J., Choi, B., 2014. Development of a piezoelectric energy harvesting system for implementing wireless sensors on the tires. Energy Conversion and Management 78, 32–38.

Lien, I.C., Shu, Y.C., 2013. Piezoelectric array of oscillators with respective electrical rectification, in: Sodano, H. (Ed.), Active and Passive Smart Structures and Integrated Systems 2013, International Society for Optics and Photonics. SPIE. pp. 25–32. doi:10.1117/12.2009208.

Liu, H., Zhong, J., Lee, C., Lee, S.W., Lin, L., 2018. A comprehensive review on piezoelectric energy harvesting technology: Materials, mechanisms, and applications. Applied Physics Reviews 5, 041306.

Machado, L.Q., Yurchenko, D., Wang, J., Clementi, G., Margueron, S., Bartasyte, A., 2021. Multi-dimensional constrained energy optimization of a piezoelectric harvester for e-gadgets. iScience 24.

Maghsoudi Nia, E., Wan Abdullah Zawawi, N., Mahinder Singh, B., . Design of a pavement using piezoelectric materials. Materialwissenschaft und Werkstofftechnik 50, 320–328. doi:https://doi.org/10.1002/mawe.201900002.

Peigney, M., Siegert, D., 2013. Piezoelectric energy harvesting from traffic-induced bridge vibrations 22, 095019.

Peng, Y., Xu, Z., Wang, M., Li, Z., Peng, J., Luo, J., Xie, S., Pu, H., Yang, Z., 2021. Investigation of frequency-up conversion effect on the performance improvement of stack-based piezoelectric generators. Renewable Energy 172, 551–563. doi:https://doi.org/10.1016/j.renene.2021.03.064.

Peralta, P., Ruiz, R., Natarajan, S., Atroshchenko, E., 2020. Parametric study and shape optimization of piezoelectric energy harvesters by isogeometric analysis and kriging metamodeling. Journal of Sound and Vibration 484, 115521. doi:https://doi.org/10.1016/j.jsv.2020.115521.

Piliposian, G., Hasanyan, A., Piliposyan, D., 2019. The effect of the location of piezoelectric patches on the sensing, actuating and energy harvesting properties of a composite plate. Journal of Physics D: Applied Physics 52, 445501. doi:10.1088/1361-6463/ab37be.

Pozo, B., Garate, J.I., Araujo, J.A., Ferreiro, S., 2019. Energy harvesting technologies and equivalent electronic structural models—review. Electronics 8.

Priya, S., 2007. Advances in energy harvesting using low profile piezoelectric transducers. Journal of Electroceramics 19, 167–184. doi:10.1007/s10832-007-9043-4.

Ramezanpour, R., Nahvi, H., Ziaei-Rad, S., 2016. Electromechanical behavior of a pendulum-based piezoelectric frequency up-converting energy harvester. Journal of Sound and Vibration 370, 280–305. doi:https://doi.org/10.1016/j.jsv.2016.01.052.

Sagentia, 2011. Energy Harvesting [White paper]. Technical Report. URL: `https://www.sagentia.com/files/2015/12/Energy-Harvesting.pdf`.

Sezer, N., Koç, M., 2021. A comprehensive review on the state-of-the-art of piezoelectric energy harvesting. Nano Energy 80, 105567.

Shirvanimoghaddam, M., Shirvanimoghaddam, K., Abolhasani, M.M., Farhangi, M., Zahiri Barsari, V., Liu, H., Dohler, M., Naebe, M., 2019. Towards a green and self-powered internet of things using piezoelectric energy harvesting. IEEE Access 7, 94533–94556.

Sisinni, E., Saifullah, A., Han, S., Jennehag, U., Gidlund, M., 2018. Industrial internet of things: Challenges, opportunities, and directions. IEEE Transactions on Industrial Informatics 14, 4724–4734.

Usman, M., Hanif, A., Kim, I.H., Jung, H.J., 2018. Experimental validation of a novel piezoelectric energy harvesting system employing wake galloping phenomenon for a broad wind spectrum. Energy 153, 882–889.

Wang, J., Yurchenko, D., Hu, G., Zhao, L., Tang, L., Yang, Y., 2021. Perspectives in flow-induced vibration energy harvesting. Applied Physics Letters 119, 100502.

Yurchenko, D., Machado, L.Q., Wang, J., Bowen, C., Sharkh, S., Moshrefi-Torbati, M., Val, D.V., 2022. Global optimisation approach for designing high-efficiency piezoelectric beam-based energy harvesting devices. Nano Energy 93, 106684.

Yurchenko, D., Val, D.V., Lai, Z.H., Gu, G., Thomson, G., 2017. Energy harvesting from a DE-based dynamic vibro-impact system. Smart Materials and Structures 26, 105001.

Zhang, C., Lai, Z., Li, M., Yurchenko, D., 2020. Wind energy harvesting from a conventional turbine structure with an embedded vibro-impact dielectric elastomer generator. Journal of Sound and Vibration 487, 115616. doi:https://doi.org/10.1016/j.jsv.2020.115616.

Zhou, X., Parida, K., Halevi, O., Liu, Y., Xiong, J., Magdassi, S., Lee, P.S., 2020. All 3d-printed stretchable piezoelectric nanogenerator with non-protruding kirigami structure. Nano Energy 72, 104676.

Appendix A. Governing device's equations and relationships

Appendix A.1. Governing equations of motion

Throughout this paper it is assumed that the PE beams are all identical and vibrate at the fundamental (first) natural frequency. The electromechanical model used in this study is taken from Machado et al. (2021) and modelled in Matlab/Simulink:

$$\begin{aligned} &\frac{d^2\eta_r(t)}{dt^2} + 2\zeta\omega_r \frac{d\eta_r(t)}{dt} + \omega_r^2 \eta_r(t) + \alpha_r\, v(t) = N(t) \\ &C_p \frac{dv(t)}{dt} + \frac{v(t)}{R_l} = \sum_{r=1}^{\infty} \alpha_r \frac{d\eta_r(t)}{dt}, \end{aligned} \tag{A.1}$$

where $N(t)$ is the force applied to the beam. Since they operate under free vibrations we have that $N(t) = 0$. C_p is the capacitance of the beam while α_r is the electromechanical coupling term, respectively expressed in Equations A.2 and A.3:

$$C_p = \varepsilon_{33}^S \frac{w_p l_p}{t_p}, \tag{A.2}$$

$$\alpha_r = -Y_p d_{31} w_p t_{pc} \left. \frac{d\phi_r(x)}{dx} \right|_{x_1}^{x_2}, \tag{A.3}$$

where Y_p is the Young's modulus of the PE layer, considering a constant electrical field.

Appendix A.2. Constants, Variables and Constrains

In the design process of the harvester, is it essential to consider all the parameters that play a part in its performance. These parameters are categorised into constants, variables and constraints, being possible change their categories depending on the application. The constants are values established prior to the optimisation process and are not affected by it, e.g., the PE material constants and device's sizes. The variables are the parameters directly affected by the optimisation whose values are optimised towards high performance, e.g., e.g. the size and thickness of the PE beam's substrate. The constraints are pre-defined conditions imposed to the optimisation algorithm as boundaries, equalities or inequalities, written as mathematical

Table A.6: Parameters related to the design of the energy harvester classified into constants, variables and constraints

Constants	Variables	Constraints
Device Dimensions L_d, W_d, t_d	Beam's Tip Displacement δ	Maximum Beams Stress σ_{max}
PE Mechanical Constants $\rho_p = 4700\ kg/m^3$ $Y_p = 169\ GPa$ $t_p = 30\ \mu m$	Substrate Thickness t_s	Maximum Carriage Length L_{Mmax}
Substrate Mechanical Constants $\rho_s = 2330\ kg/m^3$ $Y_s = 169\ GPa$		Maximum Carriage Mass M_{max}
Beams' Length and Width $l_b = 20\ mm$, $w_b = 5\ mm$	Number of Beams, Pins, Beams Between Pins and Removed Beams n_b, n_p, n_{bbp}, $n_s^{\varnothing}$,	Max/Min Tip Displacement δ_{max}, δ_{min}
Carriage Width W_c	Carriage Mass, Length, Thickness M_c, L_c, t_c	Carriage Excitation Frequency f_c
PE Constant $d_{31} = -20\ pC/N$, $\varepsilon_r = 53.2$	Optimal Resistance, Beam Capacitance R_{opt} , C_p	Maximum Ouput Voltage V_{max}

expressions. Table A.6 presents all the parameters related to the optimisation process and classify them into the outlined categories. This table does not contain the parameters of a buck-boost DC-DC converter, which can also be optimised through the proposed algorithm.

Appendix A.3. Mathematical formulation of constrains

The following equation, derived in Machado et al. (2021), establishes the relationship between the total number of excitations and numbers of beams, pins and beams between pins:

$$n_{ex} = n_p n_b - n_p n_{bbp}(n_p - 1) \tag{A.4}$$

Given the quadratic relationship between the number of excitations and the number of plectra, the optimal number of pins is $n_p = (n_b + n_{bbp})/(2n_{bbp})$.

Equation (A.5) presents states that the length of the carriage l_M cannot exceed the length of the device l_d, and that the distance between plectra S_p needs to be equal or greater than the distance between beams S_b, i.e., there cannot be more than one plectra between two beams.

$$l_d \geq l_M, \quad S_p \geq S_b, \tag{A.5}$$

The distance between beams and the number of beam are defined as:

$$S_b = 2\delta_t + t_b, \quad n_b = \left\lfloor \frac{l_d}{S_b} \right\rfloor, \tag{A.6}$$

where $\lfloor \cdot \rfloor$ operation indicates the closest small integer.

The number of pins is selected based on the force delivered by a given mass at a given inclination angle and it is assumed to be grater than unity:

$$\begin{aligned} n_p &= \left\lfloor \frac{Mgsin\theta}{k_b \delta_b} \right\rfloor > 1, \\ k_b &= 3Y_b I_b / l_b^3, \quad I_b = \frac{w_b t_b^3}{12}. \end{aligned} \tag{A.7}$$

The number of the beams between pins is defined as follows:

$$S_p = \frac{(l_M - S_b)}{(n_p - 1)}; \quad n_{bbp} \leq \left\lfloor \frac{L_p}{S_b} \right\rfloor. \tag{A.8}$$

The stress ratio between the experienced stress and the maximum stress is given by Equation (A.9):

$$\Sigma = \sigma / \sigma_{max}, \quad \text{where} \quad \sigma_{max} = 0.75\sigma_y. \tag{A.9}$$

The total number of excitation is given by (A.4) and the electrical energy generated can be expressed as:

$$E_{total} = \sum_{n=1}^{n_b} \left(\int_{t_1}^{t_2} \frac{\boldsymbol{V}_n^2(t)}{R} dt \right), \tag{A.10}$$

where $t_2 - t_1$ is a time required for each beam's vibrations to decay to 0.85%.